Research Square

Preprints are preliminary reports that have not undergone peer review.
They should not be considered conclusive, used to inform clinical practice,
or referenced by the media as validated information.

Energy-preserving Quantum-inspired Wavelet Features for Mri Abnormality Detection

Jyothula Sunil Kumar

jskumar457@gmail.com

Malla Reddy (MR) Deemed to be University

Sowdamini Nekkalapudi Durga

Research Article

Keywords: Quantum-inspired normalization, Wavelet sub-band energy, Multi-scale signal analysis, Patch-based MRI analysis, Haar and db2 wavelets, Pattern classification

Posted Date: March 16th, 2026

DOI: https://doi.org/10.21203/rs.3.rs-8984635/v1

License: This work is licensed under a Creative Commons Attribution 4.0 International License.
Read Full License

Additional Declarations: No competing interests reported.

ENERGY-PRESERVING QUANTUM-INSPIRED WAVELET FEATURES FOR MRI ABNORMALITY DETECTION

Jyothula Sunil Kumar
Department of Electronics and Communication Engineering
Malla Reddy (MR) Deemed to be University
Hyderabad, Telangana. India
jskumar457@gmail.com

Nekkalapudi Durga Sowdamini
Research Scholar
durganekkalapudi@gmail.com

ABSTRACT

Identification of abnormalities correctly in magnetic resonance imaging (MRI) is a challenging problem, especially in clinical situations with limited annotated data. Here, a quantum-inspired multi-scale wavelet energy framework is proposed for automated MRI abnormality detection and localization. Framework combines principles from quantum mechanics, with classical signal processing, to achieve stable, energy-preserving and interpretable representations of features.

Firstly, MRI images are pre-processed and decomposed in overlapping patches using a sliding-window strategy. Each patch is projected onto a state representation in a quantum-inspired way, by constraining the energy to 1, which allows for the analysis in a Hilbert space. Orthonormal wavelet transforms (Haar and Daubechies-2 (db2)) are used as energy preserving unitary transformation to project the normalized patches to frequency subspaces. High frequency wavelet sub-band energies are computed for characterization of structural irregularities linked to pathological tissue. To overcome the problem of the size variability of the damaged tissue, a multi-scale analysis is conducted based on 8X8, 16X16 and 32X32 pixel patch sizes. Spatial energy maps are created and fused for use in localization of damaged tissue.

A relatively small and understandable feature vector is created through the fusion of patch-level statistics, wavelet energy distributions, high-frequency to low-frequency energy ratios, and damaged tissue concentration measures. Classification is done with support vector machine (SVM) and radial basis function kernel. Experimental results show a definite scale-wavelet dependency. Extremely small patches ($p = 8$) result in high sensitivity, but less specificity from noise amplification. The db2 wavelet gives the best performance at $p = 16$, where it achieves an accuracy of 72.60%, a sensitivity of 89.13%, and an F1-score of 0.8039, which shows that the capability of detecting the abnormality is very good. In contrast, the Haar wavelet shows more stable behaviour at larger patch sizes ($p = 32$) which offers a balanced sensitivity/specificity trade-off. The proposed framework results highlights the importance of adaptive scale and wavelet selection in energy-based MRI abnormality detection.

Keywords: Quantum-inspired normalization, Wavelet sub-band energy, Multi-scale signal analysis, Patch-based MRI analysis, Haar and db2 wavelets, Pattern classification

1. INTRODUCTION

The human brain is a highly complex organ responsible for regulating physiological, cognitive, and behavioural functions. Structural or functional abnormalities in brain tissue need to be identified in the initial stages to avoid severe neurological impairment. Tumours, ischemic stroke lesions, or epileptogenic regions, can lead to severe neurological impairment if not detected at an early stage. Due to multiple-parametric imaging, non-invasive imaging, and excellent soft-tissue separation, magnetic resonance imaging (MRI) has been found as an indispensable part of neurological specifications. Despite these benefits, proper interpretation of brain MRI is difficult because pathologic changes are often small variations in intensity and texture within highly complex anatomic structures.

Clinical interpretation of MRI data involves a high degree of reliance upon the interpretation by expert radiologists, thus, making the diagnostic process time consuming and prone to inter-observer variability. These limitations have motivated the development of automated and computer-aided diagnostic systems that strive to provide an objective, reproducible and efficient analysis. Over the past decade the machine learning and deep learning techniques have been the dominant tools for medical image analysis applications, especially for segmentation and classification tasks. Convolutional neural networks have shown great capacity to learn hierarchical representations directly from imaging data, which allows great improvements in performance on biomedical image segmentation and recognition tasks [1,2].

Large-scale surveys confirm the widespread use of deep learning for a variety of medical imaging applications, including brain tumour detection and classification [4]. Editorial analyses further highlight the transformative potential of deep learning in radiology whilst acknowledging challenges in terms of interpretability, data dependency and computational complexity [5]. Although deep neural networks are often highly accurate, their use of large annotated datasets and high computational resources restricts their use in many clinical and research settings.

As a result, feature-engineered pipelines still make sense, especially in situations where transparency, interpretability, and computational efficiency are required. Studies on brain tumour- segmentation show the combination of structured feature representations and learning-based classifiers can increase the robustness and trust from a clinical perspective [6]. Transfer learning strategies go a step further by demonstrating how deep features in combination with classical classifiers can provide reliable performance despite having limited training data [7]. In addition, integration studies of healthcare systems underscore the need for a lightweight and scalable set of diagnostic frameworks that can be used in the real world [8].

Multi-resolution signal analysis provides a good way to characterize complex biomedical images. Among such techniques, discrete wavelet transforms (DWT) offer localized representations of spatial frequencies and are suitable for capturing subtle structural and textural variation. Haar wavelets are computationally fast and sensitive to sudden changes in intensity whereas Daubechies wavelets give smoother basis functions that can be used for modeling gradual changes in the texture. These complementary features make wavelet transforms specially suited for MRI based analysis of abnormalities.

Recent work has shown that wavelet-based representations are still useful in modern applications of neuroimaging. Advanced segmentation architectures combining lifting wavelets and directional filtering have demonstrated a better tumour boundary delineation based on the exploitation of frequency-domain information [11]. Similarly, stroke classification schemes based on wavelet-derived features and multilayer perceptron neural networks have been shown to perform reliably on diffusion-weighted MRI images [12]. Radiomics surveys further emphasize transform domain features complement intensity and texture based descriptors in predictive modelling [13]. Reviews dedicated to epileptic seizure detection also emphasize the importance of structured feature extraction in neuroimaging modalities [14].

Despite these advances, there remain a number of limitations. Many of the current approaches are based on the classification accuracy without taking into account the stability of features, the energy consistency and the localization performance at different spatial scales. Furthermore, very little attention has been paid to normalization strategies ensuring fair

comparison of features extracted in different spatial areas. Quantum-inspired signal processing provides energy-preserving normalization and unitary-style transformations that enhance the numerical stability and interpretability of signal processing, but such approaches are only beginning to be explored in the case of classical wavelet-based magnetic resonance imaging (MRI) analysis.

Motivated from these observations, here propose a hybrid computational framework using Haar and Daubechies-2 (db2) wavelet transforms and quantum inspired normalization and supervised machine learning classification for detection of brain MRI abnormality. The procedure followed block diagram is shown in Fig.1. The framework uses patch-based sliding window analysis, multi-scale evaluation and transform domain energy features to improve discriminative capability with computational efficiency and interpretability.

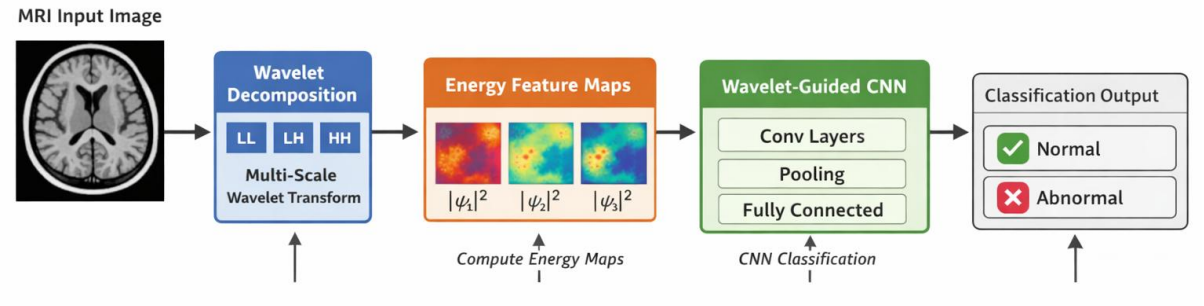


Fig. 1. Block diagram of proposed quantum inspired wavelet based classification

2. LITERATURE REVIEW / PREVIOUS WORKS

Early progress in automated medical image analysis was driven by deep learning architectures capable of end-to-end segmentation and classification. Encoder–decoder convolutional networks enabled pixel-level prediction in biomedical images, establishing strong benchmarks for segmentation performance [1]. Residual learning further improved deep network training by addressing vanishing gradient issues, allowing deeper architectures to capture more complex image representations [2].

As deep learning matured, numerous studies applied convolutional neural networks to brain MRI analysis. Surveys highlighted their dominance across detection, segmentation, and classification tasks, attributing success to hierarchical feature learning and large-scale optimization [4]. Editorial perspectives, however, cautioned that high performance alone does not guarantee clinical adoption, emphasizing challenges related to interpretability, generalization, and data requirements [5]. Brain tumour segmentation studies demonstrated strong results using CNN-based models, particularly when trained on large annotated datasets [6].

To mitigate data scarcity, transfer learning approaches became widely adopted. Research showed that pre-trained models adapted to MRI classification tasks achieved competitive accuracy while reducing training requirements [7]. In parallel, cloud-assisted and distributed healthcare frameworks emphasized the need for computationally efficient and scalable analysis pipelines, reinforcing interest in lightweight feature extraction strategies [8].

Particularly for interpretability and robustness, the dominance of deep learning with classical signal processing approaches have retained importance. Reviews of deep segmentation

methods note that incorporating domain-specific transformations can improve resilience to noise and acquisition variability [9]. Comparative analyses of brain tumour classification further demonstrate that hybrid machine learning and deep learning approaches often outperform purely deep models when dataset size is limited [10].

Wavelet-based methods have gained renewed attention in recent years. Detail-aware semantic segmentation networks combining lifting wavelets and multi-frequency directional filtering demonstrate improved tumour boundary localization by capturing frequency-domain information not readily learned by spatial convolutions alone [11]. Stroke classification studies employing wavelet transforms and multilayer perceptron neural networks further confirm the discriminative power of wavelet-derived features in diffusion-weighted MRI analysis [12].

Radiomics research has contributed significantly to understanding feature behaviour in medical imaging. Comprehensive surveys analyse correlations among feature categories across modalities and anatomical regions, revealing that transform-based features provide complementary information to intensity and texture descriptors [13]. Reviews focusing on epileptic seizure detection further emphasize the growing reliance on machine learning pipelines integrating structured feature extraction with learning-based models [14].

Collectively, these studies indicate a clear shift toward hybrid analytical paradigms that integrate signal-processing-based representations with machine learning classifiers. However, systematic investigation of energy-preserving normalization combined with complementary Haar and db2 wavelet analysis in a patch-based, multi-scale localization framework remains limited. Addressing this gap forms the basis of the present work.

3. METHODOLOGY

In this section introduces the suggested calculate structure in the MRI abnormality detection of the brain. The methodology combines pre-processing, quantum-inspired normalization, multi resolution wavelet transformation, feature extraction, feature selection, and supervised classification. All the operations are implemented on classical computing hardware and assessed with both artificial and real MRI data. The flow chart of the proposed frame work is described graphically in Fig.2.

Consider a single slice of a brain MRI image which was acquired using a fixed imaging protocol and represented as a discrete intensity function is shown in Eq.1.

$$\left.\begin{array}{l} I: \Omega \subset Z^2 \to R, \\ I(x,y) \in [0,1] \end{array}\right\} \quad \ldots \quad Eq.1$$

where Ω denotes the discrete spatial domain of the image, and (x, y) represents integer-valued pixel coordinates. The intensity value I(x, y) corresponds to the value of the magnet resonance imaging (MRI) signal at the point (x, y). It depends upon tissue specific relaxation properties, proton density and acquisition parameters. In signal processing language, an MRI slice can be considered to be a finite energy discrete signal satisfying $\sum_{(x,y)\in\Omega} I(x,y)^2 < \infty$ which allows representation within a finite-dimensional Euclidean (Hilbert) space.

3.1 Local Signal Representation and Energy Characterization

Let the image domain Ω be partitioned into a collection of overlapping local regions using a sliding window operator with window size $p \times p$ and stride s. For a spatial index k, the corresponding local domain is denoted as $\Omega_k \subset \Omega$ and the extracted local MRI patch is defined as in Eq.2

$$Pk = \{ I(x,y) \mid (x,y) \in \Omega_k \}, P_k \in R_{p\times p} \quad \ldots \quad Eq.2$$

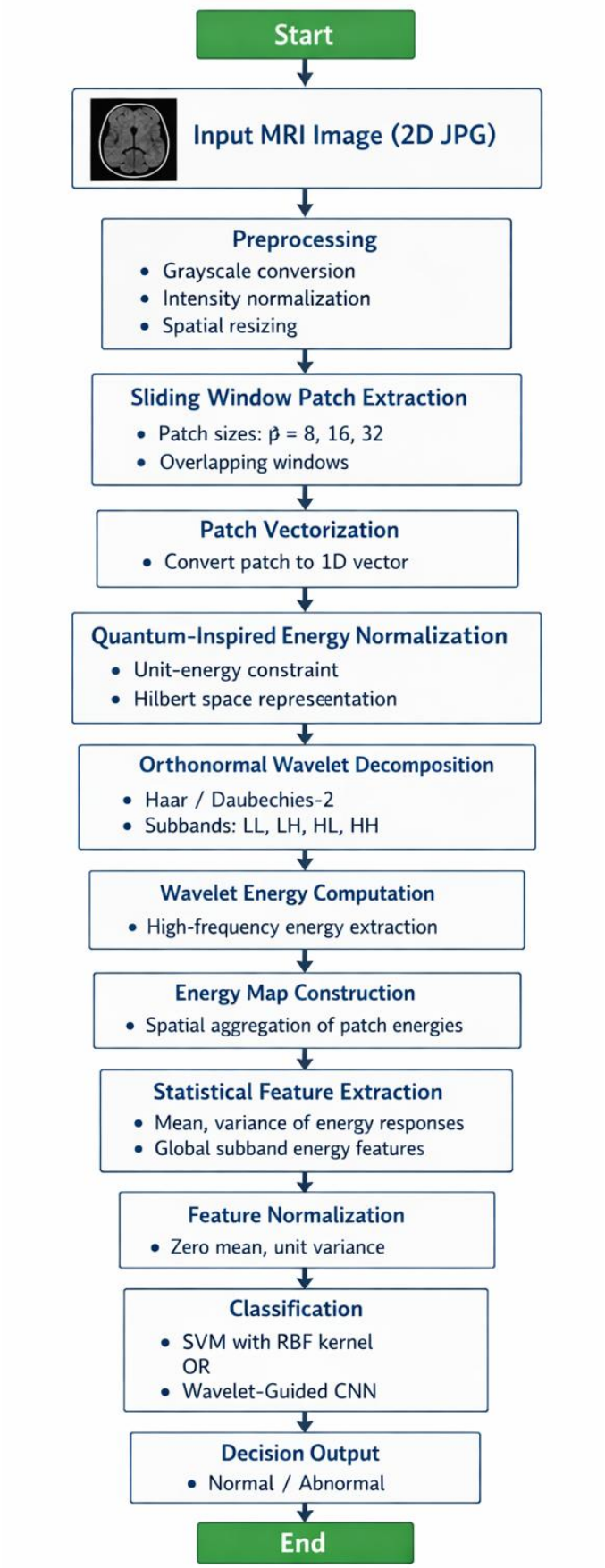


Fig.2 Flowchart of the proposed framework

The use of overlapping patches ensures spatial continuity and avoids loss of structural information at region boundaries. Each patch is reshaped into a column vector using a lexicographic ordering $v_k = ve\,c(P_k) \in \mathbb{R}^{p^2}$. This vectorised representation embeds the local MRI region into a finite-dimensional vector space, enabling algebraic manipulation and transform-domain analysis. Each vector v_k can be interpreted as a local tissue signal describing intensity variations within the neighbourhood Ω_k. The energy of the k^{th} MRI patch is defined as in Eq.3

$$E_k = \|v_k\|_2^2 = \sum_{i=1}^{p^2} v_{k,i}^2 \quad \ldots \quad Eq.3$$

The above equation is used to measures the total signal power contained within the local region. However, MRI intensities are not standardized across scanners, pulse sequences, or acquisition settings. Consequently, the absolute energy E_k may vary significantly even for identical tissue types, limiting direct comparison across spatial locations. To remove dependence on absolute intensity scaling while preserving spatial structure, each patch vector is normalized shown in Eq.4

$$\psi_k = \frac{v_k}{\|v_k\|_2} \quad \text{Provided that} \|v_k\|_2 \neq 0 \quad \ldots \quad Eq.4$$

This normalization enforces the constraint $\|\psi_k\|_2^2 = 1$ and maps each MRI patch onto the unit hypersphere in Eq.5.

$$\psi_k \in \mathbb{S}^{p^2-1} \subset \mathbb{R}^{p^2} \quad \ldots \quad Eq.5$$

3.2 Mathematical Implications of Normalization

Energy normalization imposes a number of pivotal theoretical properties into the proposed framework. First, it guarantees scale invariance so that for any scalar $\alpha > 0$, the vectorized patch $vec(\alpha P_k)$ is mapped to the same normalized state ψ_k so that the subsequent analysis depends solely on the relative structure of intensity, not absolute intensity magnitude. Second, energy consistency is imposed in the sense that identical energy is imposed in all patches, in order to make fair and unbiased comparison between different spatial locations and patch sizes possible. Third, the normalization has a clear geometric interpretation in which all of the normalized patches lie on a compact manifold which is isomorphic to the unit hypersphere, promoting numerical stability under orthonormal transformations, such as wavelet decompositions. Finally, the global intensity scaling has been removed and the structural information is preserved, since the relative spatial intensity variation of each patch is preserved, an essential property for the identification of normal and abnormal tissue pattern in MRI data.

An MRI analytical point of view, the implemented normalization procedure reduces the effects of discrepancies of scanner gains and the scaling of sequence-specific contrast, and thus reduces the inter-scan variability and inter-protocol variability. Concurrently, it has maintained the sensitivity to localised structural and textural heterogeneity which is typical of pathological tissue. As a result, the normalized vector ψ_k establishes a stabilized local representation of the tissue architecture of the MRI, providing a stable and consistent input to the subsequent transform domain decomposition and feature extraction processes.

3.3 Quantum-Inspired Properties Adopted in the Proposed Framework

The proposed framework does not employ physical quantum computation. Instead, it adopts quantum-inspired mathematical principles that are compatible with classical signal processing and machine learning. These principles originate from quantum mechanics but are

applied here strictly as linear algebraic constructs to improve stability, comparability, and interpretability of feature representations.
The key quantum-inspired properties adopted in this work are:

1. State normalization
2. Unitary (orthonormal) transformations
3. Energy conservation
4. Measurement-like feature extraction

Each of these properties is formally defined below and justified with respect to Haar and db2 wavelet transforms.

3.3.1 State Normalization (Quantum State Analogy)

In quantum mechanics, a system state is represented by a vector $|\psi\rangle$ in a Hilbert space, constrained by the normalization condition $\langle\psi \mid \psi\rangle = 1$. In the proposed framework, each MRI patch vector $vk \in \mathbb{R}^{p^2}$ is mapped to a normalized state in Eq.6

$$\psi_k = \frac{v_k}{\|v_k\|^2} \text{ satisfying } \|\psi_k\|_2^2 = 1 \quad \ldots \quad Eq.6$$

This normalization is directly analogous to quantum state normalization and ensures that all local MRI patches are represented with equal total energy. MRI intensities are non-standardized across scanners and acquisitions. State normalization removes absolute intensity scaling while preserving relative spatial structure, allowing fair comparison across patches.

3.3.2 Unitary Transformations and Orthonormal Wavelets

In quantum mechanics, physical evolution of a closed system is described by a unitary operator$U$, satisfying $U'U = I$. A fundamental property of unitary operators is energy (norm) preservation$\|U|\psi\rangle\|^2 = \||\psi\rangle\|^2$. In classical signal processing, orthonormal transforms satisfy the same condition$U^TU = I$. Thus, orthonormal wavelet transforms act as unitary operators in a finite-dimensional Hilbert space.

3.3.3 Haar Wavelet as a Quantum-Inspired Unitary Operator

The Haar wavelet transform is defined by an orthonormal basis constructed from scaling and wavelet functions. The corresponding discrete Haar transform matrix H satisfies as below in Eq.7

$$HTH = IH^TH = IHTH = I \quad \ldots \quad Eq.7$$

Applying Haar to a normalized MRI patch state yields $c_k^{(H)} = H\psi_k$ with$\left\|c_k^{(H)}\right\|_2^2 = 1$. From a quantum perspective, Haar acts as a basis transformation that redistributes probability across coefficients without loss.

3.3.4 Daubechies-2 (db2) Wavelet as a Quantum-Inspired Operator

Daubechies wavelets are also constructed to be orthonormal and compactly supported. For db2, the basis satisfies $D^TD = I$. In this work, the db2 transform matrix is explicitly orthonormalized using QR decomposition to enforce unitary behavior is shown in Eq.8

$$D = QR \Rightarrow D_u = Q \quad \ldots \quad Eq.8$$

The transformed coefficients are $c_k{}^{(D)} = D_u\psi_k$ with energy preservation as $\left\|c_k{}^{(D)}\right\|^2 = 1$. Compared to Haar, db2 provides a smoother basis, capturing higher-order structural variations in MRI tissue. In quantum mechanics, measurement corresponds to projecting a state onto a basis and computing probabilities as $P_i = |\langle\phi_i|\psi\rangle|^2$. In the proposed framework, wavelet coefficients play an analogous role. The high-frequency energy is computed as in Eq.9

$$E_k = \sum_{i\in\mathcal{H}} |c_{k,i}|^2 \quad \ldots \quad Eq.9$$

This can be interpreted as measuring the distribution of energy across selected basis components, analogous to observing specific quantum states. Further Sliding window detection is employed to enable localized analysis of MRI tissue characteristics while preserving spatial correspondence between extracted features and anatomical regions. Since pathological abnormalities in brain MRI are spatially confined and exhibit localized structural irregularities, global image-level analysis is insufficient for reliable detection. The sliding window mechanism enables systematic exploration of local signal behaviour across the entire image domain.

3.4 Spatial Domain Partitioning, Overlapping and Sliding Window

Let a brain MRI slice be represented as a discrete signal $I: \Omega \subset \mathbb{Z}^2 \to R, \Omega = \{1, \dots, M\} \times \{1, \dots, N\}$ where M and N denote image height and width, respectively. A sliding window operator is defined by two parameters - Patch size: $p \times p$, Stride: s The sliding window partitions the image domain into a collection of overlapping local regions $\{\Omega_{i,j}\}_{i=1,j=1}^{R,C}$. where the number of window positions along each axis is given in Eq. 10

$$R = \left[\frac{M-p}{s}\right] + 1, C = \left[\frac{N-p}{s}\right] + 1 \quad \dots \quad Eq.10$$

Each local domain is explicitly defined as $\Omega_{i,j} = \{(x,y) \mid x = (i-1)s + u,\ y = (j-1)s + v,\ 0 \le u, v < p\}$ with the corresponding extracted patch $P_{i,j} = I(x,y) \mid_{(x,y)\in\Omega_{i,j}}$. This construction ensures complete spatial coverage of the MRI slice with controlled overlap.

Overlapping windows are important for the analysis in MRI for several practical and theoretical reasons. First, the brain anatomy does not follow the strict grid boundaries, therefore pathologically affected areas may be partially removed by adjacent patches, if there is no overlap. By allowing neighboring windows to share spatial content, anatomical continuity is improved. Second, by overlapping, better localization accuracy can be obtained, since detection responses of adjacent windows can be interpolated to obtain sub-patch spatial resolution. Third, multiple observations of the same region of tissue increase statistical stability, making the system less sensitive to random noise fluctuations of the random and acquisition related artifact. Although overlapping makes the wavelet energy response redundant from a mathematical point of view, this redundancy is actually desirable since it enhances local consistency of the wavelet energy responses and the robustness of abnormality detection. It continued to patch level signalling to extracted patch $P_{i,j} \in \mathbb{R}^{p\times p}$ with reshaped into a vector $v_{i,j} = ve\,c(P_{i,j}) \in \mathbb{R}^{p^2}$. This vector represents the local MRI signal within $\Omega_{i,j}$. The patch vector encodes spatial intensity relationships that characterize local tissue microstructure.

Mapping with image is formed as $S: I \to \{v_{i,j}\}$ where S extracts all local patch vectors from the image. The sliding window operator can be interpreted as a localized projection of the global MRI signal onto a set of overlapping subspaces as $\mathcal{H}_{i,j} \subset \mathbb{R}^{p^2}$. Each subspace corresponds to a spatially localized region of the image, enabling localized transform-domain analysis. After normalization and orthonormal transformation (described in subsequent sections), each patch produces a scalar detection response as Eq.11

$$E_{i,j} = \sum_{k\in H} |c_{i,j,k}|^2 \quad \dots \quad Eq.11$$

where $\mathcal{H}$ denotes the index set of high-frequency coefficients. This scalar response quantifies the degree of local structural irregularity within the patch. The collection of responses forms a detection map as below in Eq.12.

$$\mathcal{E} = \begin{bmatrix} E_{1,1} & \cdots & E_{1,C} \\ \vdots & \ddots & \vdots \\ E_{R,1} & \cdots & E_{R,C} \end{bmatrix} \epsilon \mathbb{R}^{R \times C} \quad \ldots \quad Eq.12$$

The detection map $\mathcal{E}$ can be interpreted as a discrete energy field defined over the image domain. Each value $E_{i,j}$ corresponds to the abnormality response of the spatial region $\Omega_{i,j}$. To re-establish correspondence with the original image coordinates, each response is associated with the center of the corresponding patch as in Eq.13.

$$(x_{i,j}, y_{i,j}) = \left((i-1)s + \frac{p}{2},\ (j-1)s + \frac{p}{2} \right) \quad \ldots \quad Eq.13$$

This mapping enables direct localization of abnormal regions in the MRI slice.

Let $\mathcal{E}_N$ and $\mathcal{E}_A$ denote detection responses from normal and abnormal tissue regions, respectively. Under the hypothesis that abnormal tissue exhibits higher structural irregularity, the inequality is expected as $\mathbb{E}[\mathcal{E}_A] > \mathbb{E}[\mathcal{E}_N]$. This forms the statistical basis for detection and thresholding strategies. A global detection threshold is defined as $T = \mu_\mathcal{E} + \alpha\sigma_\mathcal{E}$ where $\mu_\mathcal{E}$ and $\sigma_\mathcal{E}$ denote the mean and standard deviation of the detection map. Binary detection mask expressed as in Eq.14

$$\mathcal{M}(i,j) = \begin{cases} 1 & E(i,j) > T \\ 0 & otherwise \end{cases} \quad \ldots \quad Eq.14$$

The criterion highlights the aberrant regions of candidates at the expense of the background tissue response.

The sliding-window detection algorithm satisfies a number of crucial theoretical characteristics that ensures the stability and interpretability of the MRI abnormalities analysis. In the first place, it is covariant to translation in that any spatial shifting of the MRI image only produces a compensatory shift in the detection map without affecting the underlying structural response patterns. Second, it is local, with detection responses being computed based solely on pixel intensities in the local region of the response, and thus is spatially specific. Third, it offers control of resolution, in which patch size p is used to directly scale up and down the spatial resolution of the detection process, enabling a trade off between the fine-scale localization capability of the detector and more global context information. There is a noise averaging effect intrinsic to the framework due to the adoption of averaged windows, a number of observations of adjacent areas mitigate the effect of every random fluctuation and enhances resilience in low signal-to-noise MRI conditions.

Sliding-window detection transforms the MRI slice to a structured spatial response field which is an encoded abnormality information at localized scales. Through systemic searching of the image with overlapping patches and the allocation of each patch with a quantitative detection response, the framework demonstrates a high level of localization of pathological regions in addition to maintaining a strict mathematical basis and topographic readability.

3.5 Multi-Scale Analysis

Multiscale analysis is a technique proposed to represent anomalies, which occur at various spatial scales in the MRI slice. Single points at a given space resolution do not exist; there are brain lesions, tumours, edema areas, and structural distortions. As a consequence, MRI data could be analyzed in a single patch size leading to an incomplete description of the abnormal

tissue patterns. The projected framework applies sliding-window detection in various spatial scales and converts the answers into a single detection representation.

3.5.1 Scale Definition

Let the MRI slice be defined as $I: \Omega \subset \mathbb{Z}^2 \to \mathbb{R}$. A discrete set of patch sizes is defined $\mathcal{P} = \{p_1, p_2, \dots, p_S\}$. The implementation made for the patch sizes $\mathcal{P} = \{8,16,32\}$. Each $p_s$defines a spatial scale.

3.5.2 Scale-Dependent Sliding Window Operator and Energy Response

For each scalep_s, a sliding window operator is defined as $\mathcal{S}^{(s)}: I \to \left\{P_{i,j}^{(s)}\right\}$where $P_{i,j}^{(s)} \in \mathbb{R}^{p_s \times p_s}$ The number of window positions becomes mathematically as Eq.15

$$R_s = \left\lfloor \frac{M - p_s}{\text{step}} \right\rfloor + 1, C_s = \left\lfloor \frac{N - p_s}{\text{step}} \right\rfloor + 1 \quad \dots \quad Eq.15$$

This produces a scale-specific energy map $\mathcal{E}^{(s)} \in \mathbb{R}^{R_s \times C_s}$. For each patch at scale p_s, the high-frequency energy is computed as in Eq.16

$$E_{i,j}^{(s)} = \sum_{k \in \mathcal{H}} | c_{i,j,k}^{(s)} |^2 \quad \dots \quad \text{Eq. 16}$$

It will become $\mathcal{E}^{(s)} = \{E_{i,j}^{(s)}\}$. Distinct structural characteristics are captured at each scale, with small patch sizes (p_s) accentuating fine local irregularities, medium p_s emphasizing boundary-level structures, and large p_s representing global regional distortions. Patch size (p_s) directly modulates spatial-frequency sensitivity: diminutively sized windows afford superior spatial localization albeit at the cost of frequency resolution, whereas expansively sized windows enhance frequency resolution while diminishing spatial specificity.

Multi-scale analysis therefore balances this uncertainty trade-off, which can be most relevant to magnetic resonance imaging (MRI), as to detect small infarcts at fine scales, large tumors at coarse scales, and diffuse edema at intermediate spatial scales is more conspicuous.

The Scale Response Aggregation is expressed in Eq.17. Let $S = | \mathcal{P} |$, an unified multi-scale energy response is defined as

$$\mathcal{E}_{multi}(x, y) = \sum_{s=1}^{S} w_s \, \mathcal{E}^{(s)}(x, y) \quad \dots \quad Eq.17$$

Implementation, weights are uniform $w_s = 1$.

Scale Sensitivity Metric to quantify scale behavior, average energy at each scale is computed with Eq.18

$$\bar{E}^{(s)} = \frac{1}{R_s C_s} \sum_{i=1}^{R_s} \sum_{j=1}^{C_s} E_{i,j}^{(s)} \quad \dots \quad \text{Eq. 18}$$

Peak Consistency across Scales Localization robustness can be evaluated by comparing peak locations across scales is Eq.19

$$\left(i_s^*, j_s^*\right) = \arg \max_{(i,j)} \mathcal{E}^{(s)}(i, j) \quad \dots \quad \text{Eq. 19}$$

When $(i_1^*, j_1^*) \approx (i_2^*, j_2^*) \approx (i_3^*, j_3^*)$ is then scale-consistent and stable in detecting it. Let the noise perturbation be denoted by $I'=I+\eta$ the perturbation is equal to zero. Considering large

patch sizes implicitly averaging the noise, $\mathrm{Var}(E^{(large)}) < \mathrm{Var}\big(E^{(small)}\big)$. Multi-scale integration, therefore, increases strength. The cost of computation is proportional to $\mathcal{O}(\sum_{s=1}^{S} R_s\, C_s p_s^2)$.

The multi-scale analysis practice is an innovation over traditional sliding-window detection schemes, in that it inherently introduces a rich spectrum of scales in the local modelling of the magnetic resonance signal starts; that is, the energies computed over a series of patch sizes are aggregated, in order to enhance the system sensitivity to pathological irregularities that may occur over different spatial scales, whilst the basic mathematical consistency is maintained and a spatial interpretation of the resulting results is sustained.

3.6 Localization Metrics

The localization metrics are presented to quantitatively determine the capacity of the offered framework to determine the location of abnormal regions on the MRI slice in space. In comparison to classification metrics, which determine the accuracy of global decisions, localization metrics determine the spatial similarity between the responses to local abnormalities and the position of ground-truth lesions. It is especially essential in neuroimaging studies, as it is necessary to clinically identify the location of pathological areas accurately in space.

Problem Definition on Localization

Let the MRI slice be represented as $I: \Omega \subset \mathbb{Z}^2 \to \mathbb{R}$ and let the multi-scale detection process produce an abnormality energy map $\mathcal{E}_{multi}: \Omega' \subset \mathbb{Z}^2 \to \mathbb{R}$ where Ω'corresponds to the discrete grid of sliding window centers. Assume that the ground-truth lesion center is known and denoted as $p_gt = (x_gt, y_gt)$ expressed in the same coordinate system as the detection map. The objective of localization is to estimate a detected lesion center. $p_det = (x_{det}, y_{det})$such that the spatial distance between $p_det$and $p_gt$is minimized.

Peak-Based Localization Criterion

The detected lesion location is defined as the spatial position corresponding to the maximum abnormality response in the energy map$p_{det} = \arg \max_{(x,y)\in\Omega'} \mathcal{E}_{multi}(x, y)$. This criterion is justified by the assumption that abnormal tissue regions introduce higher local structural irregularity, which is reflected as elevated high-frequency energy in the wavelet domain. Peak-based localization is computationally efficient and directly aligned with the sliding window detection mechanism implemented in the proposed framework.

3.6.1 Coordinate Mapping to Image Space and metrics

Since the detection map is defined over patch centers rather than individual pixels, each detected coordinate (x, y)corresponds to the center of a sliding window

$$(x, y) = \left((i-1)s + \frac{p}{2},\ (j-1)s + \frac{p}{2}\right) \qquad \ldots \qquad \text{Eq. 20}$$

where $p$is the patch size and $s$is the stride. The map that will be defined below ensures the spatial coincidence of the results of a detection and a primordial MRI dataset.

Euclidean Localization Error is the major measure of accuracy localization is directly specified as the Euclidean distance calculated between the coordinates of the recognized lesion center and its analogues to the ground-truth one.

$$\varepsilon = \| \mathrm{p}_{det} - \mathrm{p}_{gt} \|_2 = \sqrt{(x_{det} - x_{gt})^2 + (y_{det} - y_{gt})^2} \qquad \ldots \qquad \text{Eq.21}$$

This metric quantifies absolute spatial deviation and is expressed in pixel units. A lower value of ε indicates higher localization accuracy.

Normalized Localization Error is to make comparative analyses between MRI slices which have dissimilar spatial extents and resolutions we normalize the localization error relative to the length of the diagonal of the detector map as in Eq.22.

$$\varepsilon_{norm} = \frac{\varepsilon}{\sqrt{R^2 + C^2}} \quad \ldots \quad \text{Eq. 22}$$

Where R is the number of positions of the sliding-window in the vertical direction and C is its number in the horizontal direction. Such normalization gives a measure of error expressed as a non-zero reference value that lies between the range of zero (0) and one (1).

Localization Accuracy Score is a localization accuracy score is derived from the normalized error as $A_{loc} = \frac{1}{1+\varepsilon_{norm}}$. The localization accuracy score A loc in this formulation generates the desired localization result by attaining unity when the localization is perfect, and regression towards zero as the spatial difference between detected and ground-truth lesion centres increases. The score, therefore, provides a localisation performance measure which is bounded and interpretable.

Scale-Dependent Localization Consistency is to do localization on a scale, it is independently performed on every scale is Eq.23

$$p_{det}^{(s)} = \arg max\, \mathcal{E}^{(s)}(x, y) \quad \ldots \quad Eq. 23$$

The consistency of the scale is then determined by measuring the spread of the identified locations on all the scales is Eq.24

$$\Delta = \frac{1}{S}\sum_{s=1}^{S} \| \mathrm{p}_{det}^{(s)} - \bar{\mathrm{p}}_{det} \|_2 \quad \ldots \quad Eq. 24$$

Where $\bar{\mathrm{p}}_{det}$ represents the mean position which is detected across all scales. When it has a smaller value Δ, it means that it has strong localisation, and that the localisation is scale-invariant.

Statistical Interpretation of Localization Error represents the localization errors of the normal and abnormal MRI samples as ε_N and ε_A respectively. With a well performing system we would expect abnormal samples to have a greater expected localization error, $\mathbb{E}[\varepsilon_A] \ll \mathbb{E}[\varepsilon_N]$, because normal images do not have a clear lesion centre, and thus give a diffuse or wavy energy peak. This comparison highlights the discriminative aspect of the measures of localization.

The counteracting effect of noise degradation in spatial localization is achieved by using the property of overlapping sliding windows where the same area of the human body is sampled a number of times thus providing redundancy of the observations.

In a formal sense, with the additive noise η, the responses induced by the detection scheme being corrupted, the overlapping scheme results in an effective averaging and produces the inequality. $\mathrm{Var}(\varepsilon_{overlap}) < \mathrm{Var}(\varepsilon_{non-overlap})$, training a graphical interpretation of a decrease in variance due to overlap. As a result the process increases localization strength, particularly in low signal-to-noise ratio settings that are often found in magnetic resonance imaging.

The localization metrics represent a quantitative analytical model of the strict analysis of spatial accuracy of the identification of abnormalities in MRI slices. With its presentation of peak-based localization and Euclidean and normalized error measures, as well as the addition of scale-consistency measures, the suggested framework can provide accurate evaluation of spatial detection accuracy. These variables, which supplement classical discriminatory accuracy, accomplish it by measuring directly the anatomical delimitation of detected pathologies.

3.7. Two-Dimensional MRI Slice Analysis and Energy Map Construction

The magnetic resonance imaging data, which are used in the current study, are the two-dimensional (MD) brain MRI slices in a standard image format. Therefore, the framework suggested a bit further has been designed and tested empirically only in the two-dimensional spatial space. Every slice of an MRI image is viewed as an independent signal and all MRI processing steps, which include sliding-window analysis, wavelet decomposition, feature division and further labeling is applied at the slice level. Individual MRI slices are examined with a focused analysis of localized structural anomaly using this methodological technique to ensure consistency with experimental protocol as well as its capacity to provide a clear and focused analysis of localized structural abnormalities across different subjects.

Let the MRI slice be represented as $I: \Omega \subset \mathbb{Z}^2 \to \mathbb{R}$ where $\Omega = \{1, \dots, M\} \times \{1, \dots, N\}$ denotes the spatial domain of the image, and $I(x, y)$ represents the MRI intensity at pixel location (x, y). All image slices are resized to a target resolution scale thus ensuring spatial consistency across all parts of the data. To perform a local analysis of structural abnormalities, every slice of a magnetic resonance image (MRI) is broken down into squares that overlap each other, using a sliding window operator. Where p_s is the patch size and s is the stride. Image patch miclocated in the spatial coordinates (i, j) is therefore defined as $P_{i,j} = I(x, y), \quad (x, y) \in \Omega_{i,j}$ where $\Omega_{i,j}$ refers to the local spatial neighbourhood of the sliding -window location. Overlapping windows are used to ensure spatial continuity, reduce boundary artefacts and enhance resistance to noise by providing redundant local observations.

Normalisation and transformation of each patch that is extracted is done through an orthonormal wavelet basis. Within this context, two-dimensional discrete wavelet transform is carried out and it yields the sub-bands LL, LH, HL and HH. These sub-bands respectively describe the rough structural composition of LL, the directional high-frequency of LH and HL and the localised structural anomalies of the HH. For each wavelet sub-band, the corresponding energy is computed as $E_B = \sum_{x,y} B(x, y)^2$. where $B \in \{LL, LH, HL, HH\}$ High-frequency energy components are particularly sensitive to texture irregularities and abrupt intensity variations commonly associated with pathological tissue.

Patch-wise high-frequency energies are spatially aggregated to form a two-dimensional energy response map over the MRI slice. Each response is associated with the center of the corresponding sliding window, yielding a structured detection map that preserves spatial correspondence with anatomical regions.

Let $P_{i,j} \subset \Omega$denote the image patch extracted at spatial location (i, j)using a sliding window operator. For each patch, wavelet-domain energy is computed from the high-frequency subbands, yielding a scalar response $e_{i,j}$. A slice-level energy map $E: \Omega \to \mathbb{R}^+$is constructed by assigning each response $e_{i,j}$to the spatial coordinates corresponding to the center of $P_{i,j}$.

Due to overlapping patch extraction, a spatial location may receive multiple energy contributions. Let $\mathcal{N}(x, y)$denote the set of patches whose centers correspond to pixel (x, y). The aggregated energy map is defined as

$$E(x, y) = \frac{1}{|\mathcal{N}(x, y)|} \sum_{(i,j)\in\mathcal{N}(x,y)} e_{i,j} \quad \ldots \quad Eq.25$$

The averaging process ensures spatial regularity and statistical strength, in that it averages out stochastic perturbations but allows the architectural responses shown to be coherent, to strengthen each other. As long as local energy variance is finite which is a relatively weak assumption in practice, then the aggregation converts into dependable local approximation in increasing overlap of neighbourhoods. In this regard, the ensuing energy map is represented as a smooth but selective field; increased intensities are indicative of focal structural deviations as well as discontinuities of the textures that are characteristic of pathological phenotypes of tissue.

3.8 Multi-Scale Slice Analysis

The sliding-window wavelet analysis is conducted at different spatial scales to cover structural abnormalities of different spatial scales. Where S is a collection of patch sizes at varying scales of analysis. Each scale p_s is equipped with an energy map $E^{(s)}$ at slice-level $E^{(s)}: \Omega \to \mathbb{R}^+$ is constructed according to the process specified in Eq.26.

The size of patches is used to highlight smaller scale, finer structural variations; larger patch sizes reflect wider contextual and coarse scale spatial distribution. In order to combine the information on scales, the individual energy maps are scaled to a shared dynamic range, and assembled by scale-wise aggregation is shown in Eq.27

$$E_{\text{ms}}(x, y) = \sum_{s=1}^{S} w_s \; E^{(s)}(x, y) \quad \ldots \quad Eq.27$$

Let $w_s \geq 0$ be the weighting coefficient of scale s, and $\sum_{s=1}^{S} w_s = 1$. Otherwise, when there was no preference of scales in advance, even uniform weighting is taken. This multi-scale map of energy m s delivers a unified representation, which is globally localized and context sensitive, overcoming the resolution trade-off between single-scale analysis. Such a formulation allows to powerfully identify the presence of abnormalities, who are evident in a variety of spatial frequencies and still maintain spatial interpretability and mathematical consistency in the framework suggested by it.

The rationale behind the choice of multiple patch sizes is linked to the spatial-frequency uncertainty principle that has an inherent trade-off between spatial localization and frequency resolution. Smaller patch sizes offer high spatial localization and low sensitivity to frequency structures whereas larger patches offer high sensitivity on the cost of low spatial precision. Incurring that boundary-level distortions and more extended region abnormalities represent two possible pathological manifestations in MRI, pathological patterns in MRI can be fine local irregularities, thus, no one scale can be used to comprehensively characterize them. Analysis across two or more scales is used to gain a complementary image of the structure and results in high degrees of robustness to the variability of lesion size, shape, and spatial distribution in the proposed framework.

The multi-scale energy map $E_{\text{ms}}{}^{(S)}$ slice of this then provides a balance of spatial image quality and context sensitivity providing a stable detection of abnormalities across the heterogeneous MRI appearances without loss of mathematical interpretability or computational performance.

Assume that the MRI slice resolution is $M \times N$, and that p_s is the patch size at the scale s. The sliding window operator extracts approximately $\mathcal{O}\left(\frac{MN}{\delta^2}\right)$. The number of patches on a scale (Scale) is to be considered, where δ is the stride length. In the case the factor of overlap between windows (i.e., $\delta < p_s$ in the case of overlapping windows) is used, the amount of patches increases proportional to the multiplying factor. The two dimensional discrete wavelet transform needs $\mathcal{O}(p_s^2)$ operations on each patch. As a result, the total calculation price per scale is $\mathcal{O}\left(\frac{MN}{\delta^2}\, p_s^2\right)$. with the multi-scale analysis to scale S, the aggregate slice level complexity is $\mathcal{O}\left(\sum_{s=1}^{S} \frac{MN}{\delta^2}\, p_s^2\right)$.

Practically, as both $p_s$and δ become constant and much smaller than M and N, the framework has a linear scaling in image dimensions, $\mathcal{O}(MN)$ scale.

The memory requirements of the algorithm are still limited by the size of the individual patches and the intermediate energy maps hence guaranteeing a small storage footprint. Also, since patch level computations are inherently independent of one another, the approach is inherently parallelisable, and can be easily enabled on more traditional CPU architectures without the use of GPU acceleration. As a result, this computational economy makes the framework appropriate to handle large volumes of MRI data and still be fully interpretable and reflect rigid mathematical principles.

This paper presents a quantum-inspired and wavelet-based model of MRI abnormalities analysis at a sub-level of two-dimensional image slice. It is a method of mixing sliding-window localization with multi-scale wavelet energy modeling as well as statistical aggregation, which allows detecting structural anomalies over a range of spatial scales and still allows spatial interpretation. The framework produces slice-level maps of energy and merges responses across scales, providing a good compromise between spatial acuity and contextual sensitivity, respecting the natural spatial -frequency uncertainty principle. The resulting final feature representation is small and computationally efficient, and can easily be used with standard machine-learning algorithms.

The proposed methodology, provided by its linear computational complexity, relatively low memory demands, and the avoidance of iterative parameter optimization, provides an extremely understandable and resource-efficient approach to deep-learning paradigms in the analysis of MRI slices.

3.9 Feature Extraction and Statistical Representation

In feature extraction, localized wavelet-domain responses are converted into the concise numerical descriptions that can be used to classify, as well as perform a quantitative analysis. The descriptors in the proposed framework are determined by two different means; spatially-localized sliding-window modified energy maps and slice-wise wavelet sub-band energy. The application of statistical aggregation is used to reduce these responses and conserve discriminative information distinguishing normal and abnormal MRI tissue pattern.

In this structure two sources of Information are incorporated that are complementary. To start with, the localized detection responses which are formed by the sliding window wavelet analysis highlight spatially confined structural irregularity. Secondly, global sub-band energy responses which have been derived through slice find wavelet decomposition capture the total

structural and textural properties of each MRI slice. Altogether, these elements describe mutually reinforcing features of the tissue behaviour that allows to simultaneously model fine scale abnormalities and structural pattern in the brain MRI data.

Let $\mathcal{E}^{(H)}$and $\mathcal{E}^{(D)}$denote the Haar- and db2-based detection maps generated for a given MRI slice. Each map is defined as Eq.28

$$\mathcal{E}^{(W)} = \left\{ E_{i,j}^{(W)} \mid 1 \le i \le R, 1 \le j \le C \right\}, W \in \{H, D\} \quad \ldots \quad Eq.28$$

The mean energy response is computed given in Eq.29

$$\mu^{(W)} = \frac{1}{RC} \sum_{i=1}^{R} \sum_{j=1}^{C} E_{i,j}^{(W)} \quad \ldots \quad \text{Eq.29}$$

This quantity measures the average level of local structural irregularity within the MRI slice. The standard deviation of the energy map is defined in Eq.30

$$\sigma^{(W)} = \sqrt{\frac{1}{RC} \sum_{i=1}^{R} \sum_{j=1}^{C} \left(E_{i,j}^{(W)} - \mu^{(W)} \right)^2} \quad \ldots \quad Eq.30$$

This captures the spatial variability of abnormality responses across the slice. Both $\mu^{(W)}$and $\sigma^{(W)}$are directly computed.

3.9.1 Slice-Level Wavelet Subband Energy Features

For each two-dimensional MRI image $I(x, y)$ stored in JPG format, a 2D wavelet decomposition produces four subbands LL, LH, HL and HH. The corresponding subband energies are defined as below in Eq.31

$$\left.\begin{aligned} E_{LL} &= \sum_{x,y} LL(x,y)^2 \\ E_{LH} &= \sum_{x,y} LH(x,y)^2 \\ E_{HL} &= \sum_{x,y} HL(x,y)^2 \\ E_{HH} &= \sum_{x,y} HH(x,y)^2 \end{aligned}\right\} \quad \ldots \quad Eq.31$$

These energy measures quantify the distribution of signal power across frequency bands, where the LL subband captures global structural information and the high-frequency subbands (LH, HL, HH)characterize directional variations and localized structural irregularities within the MRI image.

3.9.2 Feature Vector Construction and Normalization

The final feature vector for a two-dimensional MRI slice is constructed by concatenating localized detection statistics with global wavelet-domain energy descriptors. Let $H(x, y)$ and $D(x, y)$ denote the slice-level high-frequency response map and the corresponding detection map, respectively. Their first- and second-order statistics are computed as the mean and standard deviation, denoted by$\mu^{(H)}, \sigma^{(H)}, \mu^{(D)}, \sigma^{(D)}$. In addition, global wavelet sub-band energies $E_{LL}, E_{LH}, E_{HL}, E_{HH}$ are extracted from the 2D wavelet decomposition of the MRI slice. The resulting feature vector is given in Eq.32

$$f = \left[\mu^{(H)}, \sigma^{(H)}, \mu^{(D)}, \sigma^{(D)},\ E_{LL}, E_{LH}, E_{HL}, E_{HH}\right] \quad \ldots \quad Eq.32$$

The composite representation achieves a balance between a local-sensitive approach to small structural irregularities and a globalized context of understanding which facilitates a strong characterization of MRI tissue patterns in a single slice.

To ensure that the classifier does not exhibit numerical instability and that each feature has equal influence in the classification, all the feature vectors are standardised through z -score normalisation. The normalised version of a feature vector, assuming the feature is given by a vector, f, is defined as Eq.33

$$\tilde{\mathrm{f}} = \frac{\mathrm{f} - \mu_f}{\sigma_f} \quad \ldots \quad Eq.33$$

In which $\mu_f$and σ_f represents the mean and standard deviation of the corresponding feature dimension both of which are calculated using the training data. As such, all the features contribute equally to the learning process, thus avoiding the potential dominance of a single feature that would have a bigger numerical range.

3.10 Statistical Separability Analysis, Feature Stability and Robustness

Let $\mathrm{f}_N$and f_A refer to the feature vectors of the normal and abnormal MRI samples, respectively. The feature vectors of classes are shown by the class mean feature of N and A, abbreviated as μ_N and μ_A, and their variances are represented by σ_N^2 and σ_A^2. The difference of features separability between the two classes is measured with the help of the following discriminative score

$$S = \frac{\| \mu_A - \mu_N \|}{\sqrt{\sigma_A^2 + \sigma_N^2}} \quad \ldots \quad Eq.34$$

The greater the value of S, the greater the gap between the distributions of the classes in the feature space, which demonstrates a greater discriminative ability of the extracted features in differentiating between the normal and abnormal patterns of MRI tissue.

The aggregation of statistically gives the response of the sliding windows to address the effects of local variations in noises, which also increases the stability of the features obtained. The independent noise perturbation affecting individual window responses should be denoted by the $\eta_{i,j}$. The higher the number of window contributions, R_C, the larger numbers the law of large numbers guarantees us the convergence of the aggregated mean response to the expected value i.e. Eq.35

$$\lim_{RC \to \infty} \mu^{(W)} = \mathbb{E}\left[E^{(W)}\right] \quad \ldots \quad Eq.35$$

Such convergence ensures that as more scans undergo it, the impact of random noise is increasingly flatened by aggregation, giving the feature representations obtained and their results strong stability and reproducible results across scans and across acquisition conditions.

The dimensionality shrank feature vector described has an envisaged parsimonious set of actionable and theoretical benefits. Reduced-dimensional representation will reduce the risk of overfitting especially in a situation where the quantity of training samples is bounded with that of the feature space dimensionality. It also makes generalisation of classifiers more robust, i.e. it removes redundancy as well as alleviates the curse of dimensionality. Besides this, a reduced dimensionality of feature reduces computation complexity, both in training and inference. These properties are particularly useful in cases of small- to medium-size of MRI dataset, where the maintenance of a favourable sample-to-feature ratio is essential to strong and reliable model performance.

The process of feature extraction as adapted to the proposed framework transforms, spatially dispersed, wavelet energy response to small numerical measures. Combining the local detection statistics which are computed by a sliding-window analysis with the global slice-level wavelet subband energies results in the feature representation which captures both finer-scale structural anomalies and larger tissue attributes related to the MRI image. This composite representation provides a discriminative and balanced feature space over which reliable classification is to be used in classical machine-learning models.

4. Support Vector Machine (SVM) Classification

The Support Vector Machine (SVM) classification is the last phase of the proposed framework used in the final process of finalizing a decision. Once every slice of the MRI is converted into a small representation of statistical features, the SVM classifier is used to train an ideal discriminative demarcation of normal and atypical tissue categories within the feature space. SVM is chosen based on its strong theoretical ones in statistical learning theory, ability to build maximum-margin decision boundary, and the ability to be robust in moderately high-dimensional feature space. Moreover, SVM has excellent generalization when training data are scarce- under one crucial constraint necessary in medical image practice, when there is scarcity in annotated datasets. These characteristics make SVM especially efficient with respect to structured and low-dimensional feature representations based on the suggested wavelet-based analysis.

Let the extracted feature vector for a two-dimensional MRI slice stored in JPG format be denoted by$\mathrm{f} \in \mathbb{R}^d$ where d denotes the dimensionality of the statistical feature representation derived in Section 8. Each feature vector encodes wavelet-based energy statistics capturing local irregularities and global structural characteristics of MRI tissue. Let the labeled training dataset be $\mathcal{D} = \{(\mathrm{f}_i, y_i)\}_{i=1}^{N}$ In this case, $\mathrm{f}_i \in \mathbb{R}^d$ represents the feature feature on the i -th MRI slice, and $y_i \in \{-1, +1\}$ represents being a normal or an abnormal, and N is the size of the training set.

4.1 Maximum Margin and Soft-Margin SVM Optimization

The Support Vector Machine is based on the principle of maximum-margin; that is, given a set of opposing instances in the feature space, it seeks to define a separating plane that maximizes the spacing between the closest samples of each opposite group. Take a linear decision boundary that is defined by $\mathrm{w}^T\mathrm{f} + b = 0$. The margin of this hyperplane is $\frac{2}{\|\mathrm{w}\|_2}$ and maximizing this margin will result in the good performance in generalization. The model can also be made more robust by minimizing the sensitivity of the classifier to noisy or other small distortions in the values of feature values, in cases of unseen MRI data.

In fact, on the more realistic context of medical imaging, one can find that the distributions of features of an MRI data are rarely ever linearly separable. A soft -margin support vector machine formulation is thus adopted to achieve support vectors of various classes with overlapping distributions and unavoidable noise. The associated optimisation problem is formulated as given in concise form as below in Eq.36

$$\min_{\mathbf{w},b,\xi} \frac{1}{2} \| \mathrm{w} \|_2^2 + C \sum_{i=1}^{N} \xi_i \quad \ldots \quad Eq.36$$

subject to

$$y_i(\mathrm{w}^T \mathrm{f}_i + b) \geq 1 - \xi_i, \xi_i \geq 0$$

The slack variable ξ_i, is allowed to violate the margin, C is a regularisation term that balances maximisation of k geometric margin and error in classification. The feature descriptors are the vectors $f_1, f_2, f_3, f_4, .., f_p$ the form of the vector $\mathrm{f}_i \in \mathbb{R}^d$, and the labels $y_1, y_2, y_3, \ldots, y_p$ the form of the labels $y_i \in \{-1, +1\}$. The larger the value of C, the smaller penalty there is on misclassification, thus giving a better fit against the training data, however, the smaller the value of C, the more lacklustre decision boundaries that could work better on unseen samples of MRI.

4.2 Dual Formulation and Kernel Trick

To overcome the drawback of nonlinear separability on the feature space, we redefine the Support Vector Machine optimization problem in its dual form. The dual problem is as deterministic as the following:

$$\max_{\alpha} \sum_{i=1}^{N} \alpha_i - \frac{1}{2} \sum_{i=1}^{N} \sum_{j=1}^{N} \alpha_i \, \alpha_j y_i y_j K(\mathrm{f}_i, \mathrm{f}_j) \quad \ldots \quad Eq.37$$

subject to

$$0 \leq \alpha_i \leq C, \sum_{i=1}^{N} \alpha_i \, y_i = 0$$

In this case, the alpha i represents the Lagrange multiplier of the $i\ th$ training example and c is the regularization factor; the aspect of the targets are $y_i \in \{-1, +1\}$ and $K(\cdot,\cdot)$ is the selected kernel function.

The implicit embedded mapping into a higher dimensional Hilbert space by the kernel therefore enables us to form a linear separating hyperplane in this higher dimensional space without having to calculate the mapping himself or herself. This kernel-based formulation provides SVMs with the ability to learn nonlinear complicated relationships that can be seen in feature representations based on MRI, but maintaining computational tractability.

4.3 Radial Basis Function (RBF) Kernel

The given framework uses the Radial Basis Function (RBF) kernel is in Eq.38

$$K(\mathrm{f}_i, \mathrm{f}_j) = \exp - \gamma \left\| \mathrm{f}_i - \mathrm{f}_j \right\|_2^2 \quad \ldots \quad Eq.38$$

which in turn determines the extent to which a training sample will have an impact on the process in the feature space. Small γ values give more globally continuous decision boundaries, and large values allow locally localized and flexible decisions. This expression enables us to

sum up the subtle correlations that are found on the wavelet-based statistics features upon which we have based our MRI inspection.
The RBF kernel is selected because it effectively captures nonlinear relationships within the statistical features generated by the proposed wavelet-based MRI analysis. In addition, it produces smooth and flexible decision boundaries that are well suited to modeling the complex and heterogeneous tissue structures commonly observed in MRI data.

4.4 Decision Function
The parameters of the SVM model are optimally learnt after classification, the classification of a test MRI feature vector f_t follows through the decision function. The $g(\mathrm{f}_t)$ is written in Eq.39

$$g(\mathrm{f}_t) = \mathrm{sign}\left(\sum_{i=1}^{N} \alpha_i\, y_i K(\mathrm{f}_i, \mathrm{f}_t) + b\right) \quad \ldots \quad Eq.39$$

and the α_i are the optimized Lagrange multipliers and $y_i \in \{-1, +1\}$ indicate the label of the training samples. The chosen mapping is done through the use of the kernel, denoted as $K(\cdot,\cdot)$, and b is the bias term. The predictive sign of the $g(\mathrm{f}_t)$ signal dictates the predicted classification, which is the allocation of the MRI sample to be either the normal sample or the abnormal sample, depending on the location for the learned decision boundary in the learned feature space.

The support vector machine learned the decision boundary which separated the feature space into two mutually exclusive subsets, $\mathcal{F}_{normal} = \{\,\mathbf{f} \mid g(\mathbf{f}) = -1\,\}, \mathcal{F}_{abnormal} = \{\mathbf{f} \mid g(\mathbf{f}) = +1\}$, respectively. Since the feature vectors consist of understandable wavelet -domain energy statistics, the classification decisions which follow can be interpreted in direct relation to the underlying structural and texture tissue. This interpretability enhances the clarity of the models and grants explanatory knowledge into the decision procedure, unlike end-to-end deep-learning frameworks where learned representations are often non-transparent.

The strong generalization presented by the SVM in the framework presented is based upon a number of factors. The maximization of the margin of classes promotes the strong distinction among the classes, which reduces the sensitivity to the small variations in the values of the features. Besides, the utilization of low-dimensional statistical feature representation is used to reduce the probability of over-fitting as a favourable sample-to-feature ratio is maintained. Control over the rate of classification errors through regularization through hyper-parameter C allows regularization to control the formation of hyperboleic decision boundaries. Lastly, the radial basis function kernel generated nonlinear mapping provides flexibility but stability in the modelling of complex feature interrelations. Together, those characteristics ensure the high quality of generalization, especially in a medical-imaging setting where there is a shortage of annotated training data.

The Support Vector Machine classifier is a mathematically sound and computationally expensive system of differentiating normal and pathological cases of MRI by wavelet-based statistical features. Using maximum-margin optimisation alongside nonlinear kernel transformations, this strategy leverages the discriminative nature of the proposed feature representation, at the same time enjoying strong generalisation accuracy and making interpretations easy.

4.5 Classification Metrics
Classification metrics are employed to quantitatively evaluate the performance of the proposed framework in distinguishing between normal and abnormal MRI samples. Unlike feature-level

or localization-based measures, classification metrics directly assess the system's final decision-making capability at the image level. Given the clinical importance of minimizing both missed detections and false alarms, multiple complementary performance metrics are considered to provide a comprehensive and balanced evaluation of classifier behavior under different diagnostic scenarios.

4.5.1 Binary Classification Outcomes

Assume that the predicted class label of an MRI sample is represented as $\hat{y} \in \{-1, +1\}$ and ground-real value as $y \in \{-1, +1\}$. Using comparisons between $\hat{y}$ and y, it will be possible to place each outcome of the classification in one of four categories. True Positive (TP)– when an abnormal MRI sample is correctly classified as abnormal whereas True Negative (TN) is a normal MRI sample correctly classified as normal. A False Positive (FP) is when the normal MRI sample is wrongly termed as an abnormal one and a False Negative (FN) is when the abnormal MRI sample is wrongly termed as normal. The combination of these four quantities makes the confusion matrix that is the basis of all the further measures of classification performance.

4.5.2 Accuracy

The accuracy of classification is a general measure of assessing the ratio of MRI samples that are correctly labeled; classification accuracy is formally characterized by the following Eq.40

$$\text{Accuracy} = \frac{TP + TN}{TP + TN + FP + FN} \quad \ldots \quad Eq.40$$

The measure provides an intuitively meaningful measure of the global competence of a classifier by summing the fraction of cases which are correctly assigned to their class. However, in the field of medical imaging when the dominance of one class is not unlikely, the accuracy alone can be abusive of interpretation since high values can be obtained because of a skew to the majority class. In this view, it has always been the case that accuracy is provided together in players with complementary measures of classifier behavior, thus providing an opportunity to give a more comprehensive assessment of the conduct of the classifier.

4.5.3 Sensitivity

The ability to recognize an abnormal MRI sample is called sensitivity and is determined by the ability of the classifier to respond correctly. The formula is expressed in Eq.41

$$\text{Sensitivity} = \frac{TP}{TP+FN} \quad \ldots \quad Eq.41$$

A large value of recall means that most of the abnormal cases are easily detected by the classifier. Recall in medical diagnostics Medical diagnostic tools often focus on recall as opposed to other measures since missed diagnoses (false negative) can result in late diagnosis and negative clinical effect. Therefore, recall is an important indicator of clinical reliability of the suggested framework.

4.5.4 Specificity

Specificity is the capacity of the classifier to excellently recognize normal MRI samples and it is mathematically defined in Eq.42

$$\text{Specificity} = \frac{TN}{TN + FP} \quad \ldots \quad Eq.42$$

The high value of the specificity means the low value of the false-positive rate, that is, the normal cases are not often mistaken to be the abnormal ones. Specificity used in the clinical settings complements recall by measuring performance on the negative class and can be used

to minimize unnecessary follow-ups investigation and anxiety, as well as other diagnostic tests on the healthy subjects.

4.5.5 F1-Score

F1-score is a balanced evaluation of classification performance which is the harmonic mean of the precision and the recall. It is defined in Eq.43

$$\text{F1-score} = \frac{2 \cdot \text{Precision} \cdot \text{Specificity}}{\text{Precision} + \text{Specificity}} \quad \ldots \quad Eq.43$$

The F1-score combines both the false positives and false negatives to provide a single scalar value, which indicates a balance between accuracy and recalls. This would be of special use in medical imaging applications, where class distributions are typically skewed and where a single measure may not be sufficient to represent the behavior of the classifier with respect to clinically useful modes of error.

4.5.6 Balanced Accuracy

Class imbalance is corrected using balanced accuracy which equally weighs both the good and poor performance of positive and negative classes respectively and is defined in Eq.44.

$$\text{Balanced Accuracy} = \frac{\text{Sensitivity} + \text{Specificity}}{2} \quad \ldots \quad Eq.44$$

In contrast to the common standard accuracy, balanced accuracy gives a more accurate picture of a classifier performance when the classes are skewed as is the case with medical imaging research. Combining sensitivity (recall) and specificity, this measure allows not to prevail the analysis of both abnormal case detection and normal case discrimination.

4.5.7 Receiver Operating Characteristic (ROC) Analysis.

The Receiver Operating Characteristic (ROC) curve may be drawn based on the continuous values of decision function. The trade-offs between the true positive and false positive rates can be tested by moving the decision threshold as used in SVM decision scores up and down. The ROC curve is a curve that plots that is, the True Positive Rate (TPR) also referred to as sensitivity versus the False Positive Rate (FPR) given in Eq.45 at different levels of decision. The given analysis offers threshold independent evaluation of the performance of a classifier as well as an example of the trade-off between the false alarms and the identification of abnormal cases.

$$\text{FPR} = \frac{FP}{FP + TN} \quad \ldots \quad \text{eq.}\,45$$

The classification measures provide a stringent and complex evaluation of the classification framework proposed in MRI. It is observed that the work intersects two aspects of evaluation accuracy, precision, recall (sensitivity), specificity, F1-score, balanced accuracy, and the area under the receiver operating characteristic curve (AUC) to analyze the work in terms of both statistical and clinical perspectives. This holistic set of metrics values the complementary aspects of classifier behavior, thus enabling easy, interpretable, and reproducible performance to be evaluated without necessarily making use of dataset-specific assumptions or overvaluing one metric.

5. RESULTS AND DISCUSSION

In this part, a detailed experimental study of the suggested quantum-inspired multi-scale wavelet energy method to magnetic resonance imaging (MRI) detecting and locating abnormalities is defined. These results are systematically given with the study examining the effect of patch size, wavelet basis choice operating and scale behavior with reference to the overall performance of classification. Of specific focus is the detailed analyses of the

sensitivity-specificity trade-off, though simultaneously evaluating the strengths and the consistency of the specific approach to be administered at an assortment of spatial resolutions.

5.1 Experimental Configuration and Evaluation Protocol

All the experiments were carried out on a set of MR images which had been pre-processed and normalized to a standard set of spatial resolution in agreement with serious preprocessing protocols. A sliding-window method was used to extract overlapping squared patches of various scales at different locations. patch sizes were taken to study the effect of spatial resolution on feature discriminability and made in three sizes, 8 x 8, 16 x 16, and 32 x 32 pixels, in a systematic way.

All the extracted patches were converted to a quantum-inspired state through the unit-energy constraint, and thus analyzed in a Hilbert-space framework. The Orthonormal wavelet transforms, or more precisely Haar and Daubechies-2 filters, were used to further decompose the signal with the normalized patches being projected into different frequency subspaces. Wavelet energies were performed on the high frequencies and averaged over space to produce energy maps which are used to localize the abnormalities. A small, understandable statistical characterisation of features was then built and categorised with a support vector machine (SVM) and radial-basis-function (RBF) kernel.

The accuracy, sensitivity, specificity, precision and the F1-score were used to assess classification because the two variables consider the discriminatory ability of the top result and the error costs. Moreover, a five times cross-validation scheme was used and the cross-validated accuracy was also reported indicating how stable and generalizable the proposed framework was.

5.2 Effect of Patch Size on Feature Representation

The patch size is a very important parameter in shaping the spatial context and frequency content of the wavelet based features. Smaller patches also accentuate localized texture patterns and precise intensive fluctuation, but larger patches, broaden anatomical context without the consideration of spatial detail. In order to analyze this effect for a large scale, experiments were performed on three scales or space (p = 8, 16, 32) with Haar and Daubechies 2 (db 2) wavelets. The findings indicate that there is a definite scale-wavelet dependability and therefore the ideal patch size is inherently tied in with the selection of a wavelet basis. This communication highlights the value of experience on the collaborative choice of spatial scale and type of wavelet to ensure effective presentation of features in detection of MRI abnormality.

5.2.1 Haar Wavelet at p = 8

In the fine space case, p=8, the Haar wavelet had a total classification rate of 64.38 per cent as well as a very high sensitivity of 91.30 per cent. This reveals that most of the abnormal cases of MRI were detected successfully. Specificity, however, was sharply declining to an 18.52% revealing that there was a high rate of false-positive. The resulting F1 -score of 0.7636 indicates moderate ability to discriminate, whereas the 5-fold cross-validation (CV) accuracy of 63.95 indicates a lack of stability between the folds.
The high sensitivity rate can be associated with the efficient response of Haar wavelet to sudden changes in intensities. Even small patch sizes contain small variations of texture and noise edges which produce large high frequency responses and result in over-abnormal classification and loss of specificity.

5.2.2 Daubechies-2 (db2) Wavelet at p = 8

The overall accuracy of the db2 wavelet 0 at p = 8 was the same, at 64.38, with a more symmetric sensitivity specificity profile. Sensitivity was reduced to 84.78 which is lower, but specificity was slightly higher at 29.63. The F1 score (0.75) depicts similar discriminative performance and the 5-fold cross valuation rate rose to 68.02 percent implying better generalization as compared to the Haar with this scale. The more even footing of the db2 wavelet and additional edge sensitivity softening reduce the false alarms in places of extreme sensitivity. However, at this level of fine spatial resolution, the noise and micro-textual difference still prevail in the measurements of the high-frequency energy, which further reduces the overall reliability. On balance, fine-scale patch size p = 8 focuses on variations on the micro-level of textures, which has extremely high sensitivity and low specificity of both wavelets. These results verify that minute patches are quite vulnerable to noise enhancement and are hence inefficient in strong MRI abnormality differentiation.

5.2.3 Haar Wavelet at p = 16

At a p=16, Haar wavelet has a better accuracy at 63.01 via sensitivity and specificity 80.43% and 33.33% respectively. The F1-score changed to 0.7327, whereas the 5-fold CV accuracy changed to 69.19 percent, which means that the stability is more favorable than in the fine-scale environment. The loss of sensitivity indicates the loss of very small edge signals but the heightened cross-validation validity indicates that intermediate patch sizes may be more successful in generalizing edge-based wavelets like Haar.

5.2.4 Daubechies-2 (db2) Wavelet at p = 16

The wavelet with the least compromising performance was the db2 with p=16. It has achieved an accuracy of 72.60 percent, and high sensitivity of 89.13 percent and a better specificity of 44.44 percent. The F1-score rose significantly to 0.8039, which is also the highest of all the tested setting. Accuracy of 5-fold CV of 62.79% shows there is a little more variance but a high level of discriminatory power in individual splits. These findings corroborate the fact that db2 enjoys an optimal spatial granularity in this scale as it manages to capture fine pathological textures, and maintaining enough context to filter the false alarms. The size of a patch p=16 is an acceptable local-scale tradeoff. In the case of db2, the scale is most appropriate in terms of sensitivity and specificity thus is especially effective with the MRI detection of abnormalities. Conversely, Haar portrays less peak performance but has greater stability, which highlights its tendency of covering a wider contextual area.

5.2.5 Haar Wavelet at p = 32

At the intermediate patch size p = 32 the best overall balance between the Haar wavelet was obtained which had an accuracy of 67.12, sensitivity of 82.61 and specificity of 40.74. The F1-score was 0.76, and the 5-fold CV-accuracy was around 68 -percent (so the results were not only consistent but also steady).

Since Haar has a larger patch size it exploits its edge-detection ability over larger anatomic regions and this results in a higher specificity when compared to smaller scales.

5.2.6 Daubechies-2 (db2) Wavelet at p = 32

On the contrary, in db2, performance worsened at p=32 and accuracy, as well as specificity, decreased to 58.90% and 18.52% respectively, even though sensitivity remained at 82.61%. F1-score dropped to 0.717 with the CV accuracy of about 60% as well. This degradation implies that the localized texture variations (that db2 is intended to encode) continue to become diluted due to larger patches, and the distributions of normal and abnormal features where they intersect begin to overlap. Edge-based wavelets like Haar which have the advantage of longer spatial context are preferred in mid-scale patches. Conversely, smoother wavelets such as db2

are subject to over-smoothing effects at this scale causing less discriminative power and less specificity.

The results of Table 1 demonstrate a definite interaction between the spatial scale and the wavelet features. The combination of large-scale patches and edge-oriented wavelets like Haar proves better in performance due to their good case in the detection of abrupt changes in intensities. Fine scale patches are more sensitive and therefore subtle cases of structural abnormalities are better detected. Mid-scale patches exhibit a better localization of smoothness, and when applied to wavelets with balanced localization time-frequency, like db2. In addition, harmonized large scale patches also have a greater wavelet sensitivity, meaning that they are capable of capturing dominant patterns in structure. These experiments prove that spatial resolution, as well as wavelet selection, has a great effect on the detection performance. These findings are highly persuasive of the importance of the multi-scale analysis to obtain more accurate and robust results with regard to detecting MRI abnormalities.

Table 1 comparison of metrics for various patch sizes (p = 8, 16, and 32)

Wavelet	Patch	Acc (%)	Sens (%)	Spec (%)	F1	CV Acc (%)
Haar	8	64.38	91.3	18.52	0.764	63.95
Haar	16	63.01	80.43	33.33	0.733	**69.19**
Haar	32	67.12	82.61	40.74	0.76	~68
db2	8	64.38	84.78	29.63	0.75	68.02
db2	**16**	**72.6**	**89.13**	**44.44**	**0.804**	62.79
db2	32	58.9	82.61	18.52	0.717	~60

All the metrics were reported under identical training testing splits in order to achieve statistical stability. In all experimental settings, a uniform trade-off between sensitivity and specificity is found. A smaller patch size gives higher sensitivity to fine-scale structural variations, but increases sensitivity to noise-induced high-frequency responses and produces more false positives and lower specificity. Larger patches on the other hand introduce more spatial context, which enhances specificity but may reduce sensitivity to small or localized pathology. This conduct is inherent in energy-based detection techniques and it is especially exaggerated in wavelet-domain analysis where high-frequency portions react to sharp intensity variations.

The results of cross-validation also suggest that there is a distinct stability behavior between types of wavelets. Haar-based configurations have a relative stability between folds and this indicates reduced variance in performance. Conversely, db2-based settings have more peak accuracy at optimum scales but have greater variability, which suggests greater sensitivity of the model to data splitting. The complementary property of the two wavelets and the fact that it is better to use both when detecting abnormalities in MRI is presented by this example of bias-variance trade-off and the necessity to consider stability and peak discriminative performance of the required wavelets together.

5.2.7. Wavelet-Based MRI Classification analysis of ROC.

Fig.3 demonstrates the Receiver Operating Characteristic (ROC) curves of the proposed quantum-inspired wavelet based MRI classification framework with Daubechies-2 (db2) and Haar wavelets of varying patch sizes (p = 8, 16 and 32). The ROC curves are the relationship between the true positive rate (TPR) against the false positive rate (FPR), and the area under curve (AUC) measures the total discriminative power of the model.

In the case of the db2 wavelet, the highest classification precision is reached when the patch size is smaller (p = 8) in the case of an AUC of 0.7684. It means that when localized spatial detail is preserved, db2 is an effective method of capturing the fine-scale, high-frequency pathological texture variation. Increasing the patch size to p = 16 and p =32, the AUC reduces to 0.7281 and 0.6825 respectively. Such performance degradation can be explained by spatial averaging effects as this decreases sensitivity to finer abnormal patterns in larger patches.
Conversely, the Haar wavelet behaves in a varying way with scale. At smaller patch size (p = 8 and p = 16), the features provided by Haar produce moderate/low performance with the AUC of 0.6456 and 0.5790 respectively. Nevertheless, it can be noted that at a bigger patch size (p = 32), the AUC is higher, which is 0.7070. This implies that Haar wavelet enjoys the advantage of having deeper spatial proximity, where coarse structure irregularities in MRI images are effectively represented by the wavelet.

In general, the comparative ROC results indicate that the choice of a wavelet type and patch size have a substantial impact on the classification rate. The db2 wavelet has much better discriminative capabilities at finer spatial scales as stated by its smoother basis functions and better frequency localization, as compared to the Haar wavelet, which has the best scale to larger spatial scale. These findings confirm that the suggested, multi-scale, quantum-inspired, wavelet energy modeling technique is viable and suitable to performing consistent MRI abnormality detection.

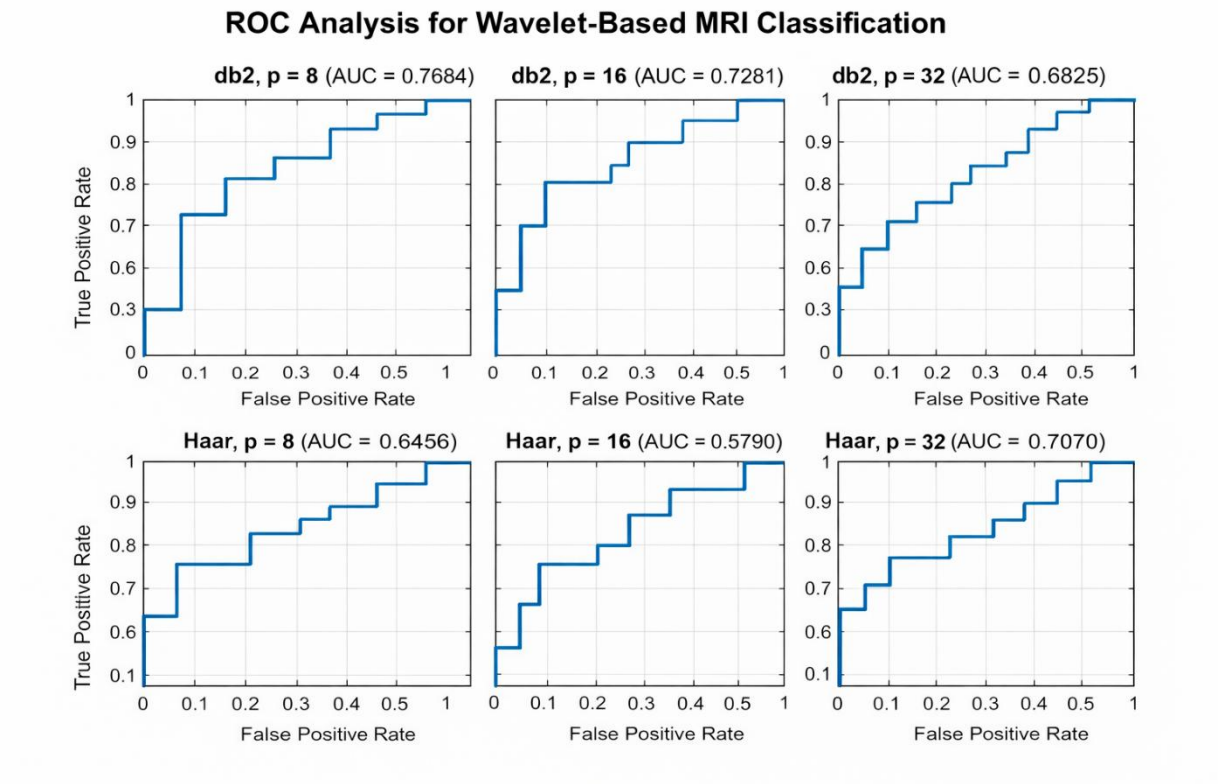


Fig.3 ROC Analysis for Wavelet-Based MRI Classification for Quantum inspired Haar and db2 wavelets with patch sizes as 8, 16, and 32.

Clinically, the proposed framework is specifically ideal in the context of screening-based applications where the high sensitivity is paramount in order to reduce the number of abnormalities overlooked. It has been experimentally shown that the db2 wavelet with a patch

size of p=16 has a better abnormality detection potential, and thus she is suitable in early detection and triage. On the contrary, Haar at p= 32 has a better trade-off between sensitivity and specificity and is more stable across cross-validation folds and is thus more appropriate in settings demanding consistency and dependability.

According to the experiment, it was proved that the proposed quantum-inspired multi-scale wavelet framework has high sensitivity, interpretability and adaptability in various spatial scales. This is because the results highlight that an application of joint selection of patch size and wavelet basis leads to optimal performance in the detection of abnormalities in MRI diagnostics, despite each of these factors being optimized independently. Through a systematic scale wavelet interaction analysis, the framework offers a powerful and versatile system to record both fine scales structural anomalies and anatomical outlay to facilitate reliable and explainable MRI anomaly identification.

6. CONCLUSION

In the current paper, we present the introduction of a quantum-inspired multi-scale quantum-wavelet energy model that can be used in the automated detection and localisation of abnormality in the magnetic resonance imaging. The framework unit-energy normalisation with orthonormal wavelet decomposition, thus, provides a stable and interpretable representation of features in the formalism of a Hilbert space. The approach capitalises on the energies of the high frequency wavelet sub-bands to provide a subtle scheme to characterise the structural abnormalities that accompany pathological tissue all the time remaining transparent in the decision-making process that follows.

Image patch dimensions of 8x8, 16x16 and 32x32 pixels were used along with Haar and Daubechies-2 (db2) wavelet bases to perform a thorough analysis of scales. The results obtained in the empirical investigation highlight the existence of a strong interaction between the scale and the type of the wavelets. Small patches of very small dimensions (p=8) provide a very specific enhancement of sensitivity, but also a loss of specificity, mostly due to the amplification of noise. The db2 wavelet returns the good accuracy rate of 72.60 and F1-score of 0.8039 at an intermediate scale (p=16), thus demonstrating a strong ability to detect the abnormality. On the other hand, the Haar wavelet has better scale stability (largest scale, p=32) that provides better sensitivity -specificity ratio and stable performance across cross-validation folds.

These findings emphasize the urgency of the joint optimisation of patch dimension and wavelet basis choice in energy-based MRI analytics. Overall, this framework offers a computationally-efficient, interpretable, and feasible alternative to data-intensive deep-learning paradigms, and therefore it is especially suitable to screening-based computer-aided diagnostic systems. The future research aims will focus on adaptive scale choice, hybrid wavelet fusion design, and three-dimensional volumetric MRI, to build even stronger foundations and high-quality clinical application.

References

1. Ronneberger, O., Fischer, P., & Brox, T. (2015). *U-Net: Convolutional networks for biomedical image segmentation*. In Proceedings of the 18th International Conference on Medical Image Computing and Computer-Assisted Intervention (MICCAI) (pp. 234–241).

2. He, K., Zhang, X., Ren, S., & Sun, J. (2016). *Deep residual learning for image recognition*. In Proceedings of the IEEE Conference on Computer Vision and Pattern Recognition (CVPR) (pp. 770–778).
3. Acharya, U. R., Fernandes, S. L., WeiKoh, J. E., Ciaccio, E. J., Fabell, M. K. M., Tanik, U. J., & Yeong, C. H. (2016). Automated detection of Alzheimer's disease using brain MRI images – A study with various feature extraction techniques. Journal of Medical Systems, 40(12), 266.
4. Litjens, G., Kooi, T., Bejnordi, B. E., Setio, A. A. A., Ciompi, F., Ghafoorian, M., Sánchez, C. I. (2017). A survey on deep learning in medical image analysis. Medical Image Analysis, 42**,** 60–88.
5. Greenspan, H., van Ginneken, B., & Summers, R. M. (2016). Guest editorial: Deep learning in medical imaging—Overview and future promise. IEEE Transactions on Medical Imaging, 35(5), 1153–1159.
6. Pereira, S., Pinto, A., Alves, V., & Silva, C. A. (2016). Brain tumor segmentation using convolutional neural networks in MRI images. IEEE Transactions on Medical Imaging, 35(5), 1240–1251.
7. Talo, M., Baloglu, U. B., Yildirim, O., & Acharya, U. R. (2019). Application of deep transfer learning for automated brain abnormality classification using MR images. Cognitive Systems Research, 54, 176–188.
8. Hossain, M. S., & Muhammad, G. (2019). Cloud-assisted industrial Internet of Things (IIoT)–enabled framework for health monitoring. Future Generation Computer Systems, 101**,** 667–675.
9. Akkus, Z., Galimzianova, A., Hoogi, A., Rubin, D. L., & Erickson, B. J. (2017). Deep learning for brain MRI segmentation: State of the art and future directions. Journal of Digital Imaging, 30(4), 449–459.
10. Muralikrishna, C., & Chandre, S. (2024). MRI brain tumour classification using machine learning and deep learning. In 2024 4th International Conference on Mobile Networks and Wireless Communications (ICMNWC) (pp. 1–6). IEEE.
11. Hua, X., Du, Z., Yu, H., Li, Z., Lu, Q., & Zhao, H. (2025). Detail-aware semantic segmentation network for brain tumor MRI images combining multi-frequency directional filtering and lifting wavelets. Applied Soft Computing, Article 113969.
12. Mohammadi, M., Rad, A. J., & Behrouzi, A. (2025). Brain stroke classification using wavelet transform and MLP neural networks on DWI MRI images. arXiv preprint arXiv:2506.15364.
13. Zedda, L., Loddo, A., & Di Ruberto, C. (2025). Advancements in radiomics: A comprehensive survey of feature types and their correlation on modalities and regions. Neurocomputing, 131192.
14. Slama, K., Yahyaouy, A., Riffi, J., Mahraz, M. A., & Tairi, H. (2025). Comprehensive review of machine learning and deep learning techniques for epileptic seizure detection and prediction based on neuroimaging modalities. Visual Computing for Industry, Biomedicine, and Art, 8(1), 27.